Bianisotropic negative-index metamaterial embedded in a symmetric medium

Zahyun Ku,[1] Keshav M. Dani,[2] Prashanth C. Upadhya,[2] and S. R. J. Brueck[1],*

[1]*Center for High Technology Materials and Electrical and Computer Engineering Department,*
University of New Mexico, Albuquerque, New Mexico 87106, USA
[2]*Center for Integrated Nanotechnologies, Los Alamos National Laboratory, Los Alamos,*
New Mexico 87545, USA
**Corresponding author: brueck@chtm.unm.edu*

In order to more clearly observe the bianisotropic effects due to fabrication-induced structural asymmetries in negative-index metamaterials based on a fishnet structure, it is necessary to measure the optical properties with symmetric substrate and superstrate bounding layers. This is accomplished in this report using an index-matching fluid and identical substrate and superstrate glass materials. © 2009 Optical Society of America
OCIS codes: 160.3918, 220.4241, 350.3618, 350.4238.

1. INTRODUCTION

For many applications, thick (multiple-functional layer) low-loss double negative-index metamaterials (NIMs) satisfying the sufficient condition ($\mathrm{Re}(\varepsilon) \equiv \varepsilon' < 0$; $\mathrm{Re}(\mu) \equiv \mu' < 0$), where ε (μ) is the permittivity (permeability), are desirable [1]. To achieve optical-frequency NIMs, the aspect ratio (height/width) needs to be large. For instance, in previous reports the NIMs based on the fishnet structure with negative refractive index at near-infrared and visible frequency were fabricated with aspect ratios of ~ 0.4 and ~ 1.4, respectively [2,3]. Present fabrication of fishnet NIMs largely employs standard semiconductor techniques: conventional lithography (interferometric, e-beam, focused-ion-beam, or nano-imprint), electron-beam evaporation, etching, and liftoff processing [2–7]. Several reports have shown that a nonnegligible sidewall angle results from this process sequence [8–10]. This sidewall angle results in a bianisotropic optical response (with different reflectivities from the substrate and superstrate directions). With the exception of the focused-ion-beam processing [5], all reported fishnet NIMs have been fabricated with a lift-off process and sequential deposition of metal and dielectric films. Because materials accumulate on the tops of the posts that define the structure, each successive film deposition has a somewhat larger aperture on the bottom metamaterial film, giving rise to a nonzero sidewall angle and to optical bianisotropy as shown in Figs. 1(a) and 1(b). This sidewall angle will vary depending on the height of the sacrificial posts and on the deposition geometry (distance from the source and collimation). Etching approaches to forming the metamaterial are also subject to top-to-bottom variations of the film stack geometry.

The negative permeability in fishnet structures is ascribed to the magnetic response from a cut-wire portion of the structure and the negative permittivity to the electric response in the thin-metal wire portion of the fishnet NIM, which together lead to a negative refractive index [11,12]. However, in a structure with a non-negligible sidewall angle, the cut-wire structure magnetic response induced by $\vec{H}$ is coupled with an electric response, and, similarly, in thin-metal wires the electric response induced by $\vec{E}$ is coupled with a magnetic response, which gives rise to bianisotropy and to differences in the reflectivity measured from the substrate and superstrate sides of the metamaterial [8,13–18]. We have previously reported on this bianisotropic behavior for an asymmetric case of a glass substrate and an air superstrate [8]. Here we extend these measurements and simulations to the symmetric case of a glass substrate, an index-matching fluid (refractive index-matching liquids, Cargille Lab, Inc.) in the metamaterial spaces, and a glass superstrate as shown in Fig. 1(c). This symmetric cladding approach provides a clearer observation of the bianisotropic characteristics resulting from the nonzero sidewall angle.

2. DESIGN AND FABRICATION

The structure of all samples reported here consists of BK7 glass substrate with one, two, or three metal–dielectric–metal functional layers with an interpenetrating two-dimensional square array of elliptical apertures. The geometrical parameters of multifunctional layered elliptical NIMs are indicated in Fig. 1(c). The orthogonal pitches of the two-dimensional gratings are both fixed at 810 nm (p). The thickness of the gold and aluminum oxide films are fixed at 25 and 58 nm, respectively. The linewidths of the gratings along $\hat{x}$, $\hat{y}$ axes are 458 and 274 nm, respectively. That is, the elliptical aperture size ($2a$, $2b$) is fixed at 536 and 352 nm ($\sim 0.66\ p$, $\sim 0.44\ p$ of the pitch for the major/minor axis).

Report Documentation Page

Public reporting burden for the collection of information is estimated to average 1 hour per response, including the time for reviewing instructions, searching existing data sources, gathering and maintaining the data needed, and completing and reviewing the collection of information. Send comments regarding this burden estimate or any other aspect of this collection of information, including suggestions for reducing this burden, to Washington Headquarters Services, Directorate for Information Operations and Reports, 1215 Jefferson Davis Highway, Suite 1204, Arlington VA 22202-4302. Respondents should be aware that notwithstanding any other provision of law, no person shall be subject to a penalty for failing to comply with a collection of information if it does not display a currently valid OMB control number.

1. REPORT DATE **04 SEP 2009**	2. REPORT TYPE	3. DATES COVERED **00-00-2009 to 00-00-2009**

4. TITLE AND SUBTITLE **Bianisotropic negative-index metamaterial embedded in a symmetric medium**	5a. CONTRACT NUMBER
	5b. GRANT NUMBER
	5c. PROGRAM ELEMENT NUMBER
6. AUTHOR(S)	5d. PROJECT NUMBER
	5e. TASK NUMBER
	5f. WORK UNIT NUMBER

7. PERFORMING ORGANIZATION NAME(S) AND ADDRESS(ES) **University of New Mexcio,Department of Electrical and Computer Engineering ,Center for High Technology Materials,Albuquerque,NM,87106**	8. PERFORMING ORGANIZATION REPORT NUMBER

9. SPONSORING/MONITORING AGENCY NAME(S) AND ADDRESS(ES)	10. SPONSOR/MONITOR'S ACRONYM(S)
	11. SPONSOR/MONITOR'S REPORT NUMBER(S)

12. DISTRIBUTION/AVAILABILITY STATEMENT
Approved for public release; distribution unlimited

13. SUPPLEMENTARY NOTES

14. ABSTRACT

15. SUBJECT TERMS

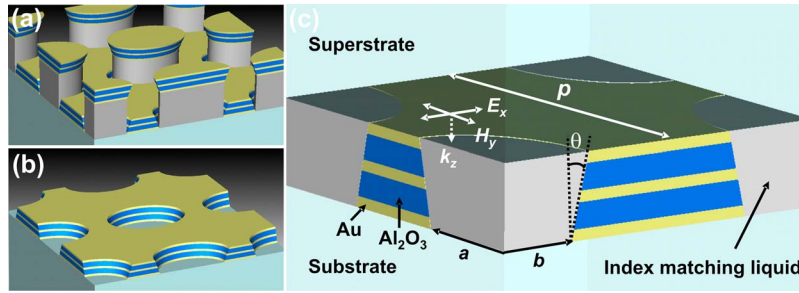| 16. SECURITY CLASSIFICATION OF:			17. LIMITATION OF ABSTRACT	18. NUMBER OF PAGES	19a. NAME OF RESPONSIBLE PERSON
a. REPORT **unclassified**	b. ABSTRACT **unclassified**	c. THIS PAGE **unclassified**	**Same as Report (SAR)**	**5**	

Fig. 1. (Color online) Schematic view of sidewall-angle formation mechanism. (a) Illustration of tendency for tops of polymer posts to be larger in e-beam evaporation of constituent materials. (b) Final structure with sidewall angle by liftoff processing. (c) Dimensions of two-functional-layered superstrate-elliptical NIM: $p = 810$ nm, $2a = 536$ nm, $2b = 352$ nm, and θ (sidewall angle) $= 13°$. The polarization direction is described (E, H, and k denote electric, magnetic field, and propagation direction, respectively).

Detailed fabrication steps for one- to three-functional-layered elliptical negative-index metamaterials were:

• 2.5×2.5 cm^2, 1-mm-thick BK7 glass was cleaned with piranha solution (4:1 volume concentration ratio of H_2SO_4 and H_2O_2) to remove any residual contamination for 10 min, followed by dehydration processing on 150°C hotplate for 6 min.

• A bottom antireflection coating layer (BARC, ~160-nm-thick, XHRIC-16, Brewer Science, Inc.) for i-line lithography was spun onto a substrate at 4K rpm for 30 s and oven baked at 175°C for 3 min; this was repeated three times to make tall posts; negative-tone photoresist (NR7-500P, Futurerex) was spread atop BARC layers at 4K rpm for 30 s and hotplate-baked at 150°C for 60 s.

• Interferometric lithography using a 355 nm third-harmonic YAG:Nd^{3+} laser source produced a periodic elliptical hole pattern in the photoresist layer with two successive orthogonal one-dimensional exposures with power 50 mJ and different doses for asymmetrical aperture shape; a 2 min post-bake at 110°C was used; the exposed and post-baked sample was developed (MF-702, Shipley, Inc.) for 13 s and rinsed with deionized water as shown in Fig. 2(a).

• After the PR pattern was defined, 25 nm Cr was deposited with an e-beam evaporator at ~10^{-7} mTorr and ~0.05 nm/s as a selective etching mask, followed by lift-off processing with acetone to remove the PR layer. This resulted in an array of elliptical Cr disks atop the BARC layer.

• An anisotropic O_2 plasma-reactive ion etch was used to transfer the Cr pattern into the BARC layer with a small isotropic etching component to provide a slight undercut for the final lift-off step as shown in Figs. 2(b) and 2(c).

• Au (25 nm)/Al_2O_3 (58 nm) were deposited alternatively by e-beam evaporation for one to three functional layers as shown in Fig. 2(d).

• Finally, an O_2 plasma ash was used to remove the BARC posts, which leads to the final structure with thickness of one to three functional layers, 108 nm, 191 nm and 274 nm, respectively. The insets of Fig. 3 show the final multifunctional layered elliptical negative-index metamaterial structures.
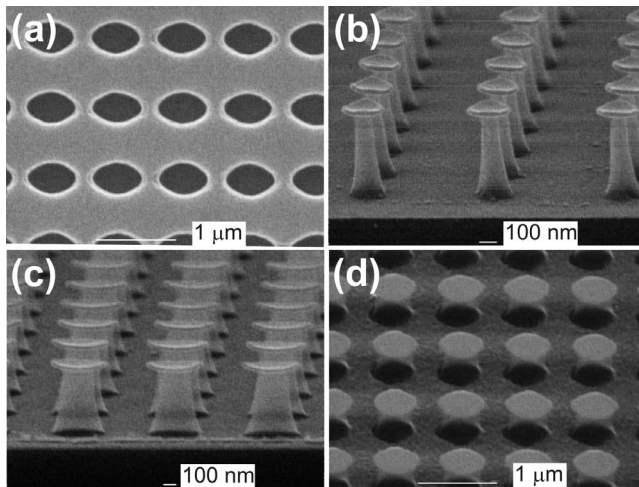

Fig. 2. Scanning electron microscope images of (a) a periodic elliptical hole PR pattern defined by interferometric lithography. (b), (c) BARC posts etched by anisotropic O_2 plasma RIE using Cr as the selective etching mask. (d) 25-nm-thick Au deposition after (b), (c).
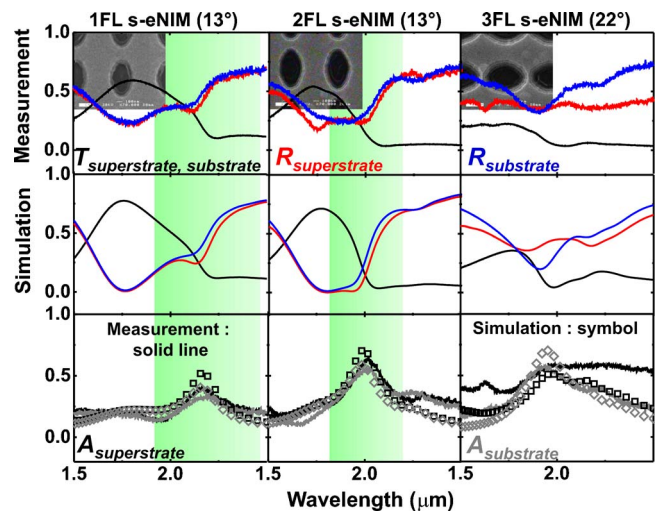

Fig. 3. (Color online) Measured/simulated transmission, reflectance (from superstrate and substrate), and absorption (1-T-R) for superstrate-elliptical negative-index metamaterials, depending on the propagation direction, with the polarization shown in Fig. 1(c). Shaded areas represent wavelength regions of negative refractive index from simulation (see below). Insets display SEM images with one- to three-functional-layered eNIMs.

3. FTIR MEASUREMENT AND SIMULATION

The transmission and reflectance from the superstrate and substrate sides were measured with a Nicolet Fourier transform infrared spectrometer (FTIR) with the specific polarization shown in Fig. 1(c), a quartz beam splitter, and a DTGS-KBr detector. The transmission was measured at normal incidence and normalized to the spectrum of a bare glass substrate. The reflectance measurement was carried out with an 11° off–normal incident beam and was normalized to the spectrum reflected from a gold mirror. The first and third rows of Fig. 3 show measured transmission, reflectance and, absorption (1-T-R) depending on the propagation direction (superstrate to substrate and vice versa) of superstrate-elliptical negative-index metamaterial (s-eNIM) with one to three functional layers.

Commercial software based on a finite integration technique (CST Microwave studio: Computer Simulation Technology GmbH, Darmstadt, Germany) was used to obtain the electromagnetic response of one- to three-functional-layered s-eNIMs depending on the propagation direction [19]. We used perfect electric conductor (PEC) and perfect magnetic conductor (PMC) boundary conditions between unit cells with $n_{substrate} = n_{superstrate} = n_{index-match\ liquid} = 1.5$, $n_{Al2O3} = 1.62$ and the Drude model for gold permittivity, where ω_p (plasma frequency) $= 9.02$ eV, ω_c (collision frequency)$= 0.081$ eV. This collision frequency is increased by a factor of three compared to that of bulk gold to account for additional scattering mechanisms in this polycrystalline thin film structure [20]. As a result of the broken structural symmetry associated with the nonzero sidewall angle ($R_{superstrate} \neq R_{substrate}$), modified retrieval methods [8,13–18] should be used to extract the effective parameters rather than the standard method associated with the symmetric structure along the propagation direction [21].

For this defined polarization, the electromagnetic response of sidewall-angled NIMs can be written as a one-

dimensional constitutive equation resulting in $D = \varepsilon_0 \varepsilon \cdot E - (i/c)\xi \cdot H$, $B = (i/c)\xi \cdot E + \mu_0 \mu \cdot H$, where c, ε_0, and μ_0 are the speed of light, permittivity, and permeability of free space. The material bianisotropy parameter ξ is related the constitutive parameters by $n^2 = \varepsilon_0 \varepsilon \cdot \mu_0 \mu - \xi^2$ [8,13–18]. The good agreement between experiment and simulation as shown in Fig. 3 gives confidence to investigating the bianisotropy effects through effective parameters.

In Fig. 4, we present the real parts of the effective parameters (n', ε', μ'), the real part of the material bianisotropy parameter (ξ'), the necessary $(\varepsilon' \cdot \mu'' + \mu' \cdot \varepsilon'' < 0)$ and sufficient conditions $(\varepsilon', \mu' < 0)$ for a negative refractive index for one- to three-functional-layered s-eNIMs with sidewall angles of 4°; 13°; and 22°. By causality $(n'' > 0)$, the negative refractive index region $(n' < 0)$ is equivalent to the region of $\varepsilon' \cdot \mu'' + \mu' \cdot \varepsilon'' < 0$. The bandwidth of the sufficient condition (shaded region) associated with a double-negative material or a negative index with lower loss becomes narrower as the sidewall-angle increases. Specifically, the region of the sufficient condition is limited by the bandwidth of the negative permeability $(\mu' < 0)$ in the case of a sidewall-angled one-functional-layered s-eNIM and a two-functional-layered s-eNIM with sidewall angles (4° and 13°), as shown in Figs. 4(a)–4(e) and it is influenced by the region of negative permittivity $(\varepsilon' < 0)$ in the case of a two-functional-layered s-eNIM with sidewall angle (22°) and all sidewall-angled three-functional-layered s-eNIMs as shown in Figs. 4(f)–4(i).

In general, the double-negative bandwidth depends primarily on the bandwidth of the resonant negative permeability; however, s-eNIMs with both two and three functional layers and larger sidewall angles as shown in Figs. 4(f)–4(h) are impacted well by the vertical shift of the negative effective permittivity due to a shifted effective plasma frequency (ω_p). In Fig. 4(i), a 22° sidewall-angled three-functional-layered s-eNIM has no region of double-negative material because the regions of negative permeability and permittivity no longer overlap. The necessary condition is also not satisfied, so the region of negative index is completely eliminated by the effects of the sidewall angle. In Fig. 4, it is obvious that effective plasma frequency (ω_p) tends to decrease as the sidewall angle increases because it is related to the fraction of space occupied by the metal plates [22]. Also, the antiresonant peak of the effective permittivity becomes weaker as the sidewall angle increases because the electric response becomes weaker, which is a consequence of the unequal size of the metal plates. The antiresonant behavior of the real part of ξ becomes stronger with an increase of the sidewall angle. At the magnetic resonance for a zero sidewall-angled (ideal) cut-wire structure, the magnetic field induces an antisymmetric current loop as shown in Figs. 5(a) and 6(a), producing a $\vec{B}$ field confined mainly between the metal plates as shown in Figs. 5(b) and 6(b). Figures 5(c) and 6(c) show that the electric field, resulting from accumulated charges at the edges of each metal plate induced by the antisymmetric currents, is expected to be antisymmetric with respect to the $y = 0$ plane, to be symmetric with respect to the xy-plane through middle of the structure, and to be confined between and near the ends of the metal plates. In a zero sidewall-angle thin-metal
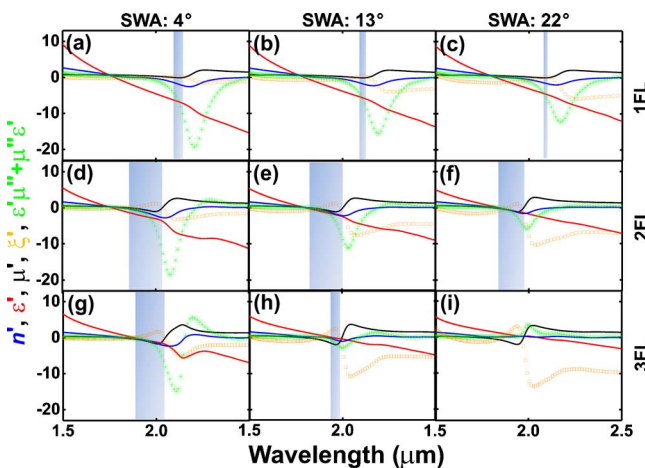

Fig. 4.   (Color online) $n', \varepsilon', \mu', \xi'$, necessary condition $(\varepsilon' \cdot \mu'' + \mu' \cdot \varepsilon'' < 0)$, and sufficient condition $(\varepsilon', \mu' < 0)$ for negative refractive index $(n' < 0)$ for one- to three-functional-layered s-eNIMs with sidewall angles (4°, 13°, 22°) are plotted. ξ' has been multiplied by 10 for clarity.
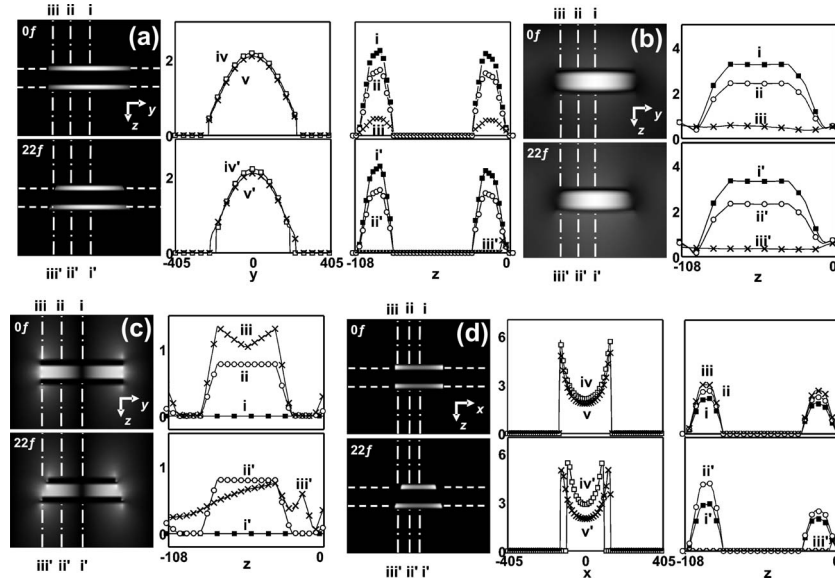
Fig. 5.   (a) Magnitude of y component of current density ($|J_y|$); (b) x component of magnetic field ($|H_x|$); and (c) z component of electric field ($|E_z|$) at a frequency of min{Re[μ_{eff}]} for one-functional-layer s-eNIM with sidewall angles (0°, 22°) are plotted along lines at the edge of cut-wire structure ($x=405$ nm). (d) $|J_y|$ along the lines in edge of thin-metal wire structure ($y=405$ nm). The values of $|J_y|$, $|H_x|$, and $|E_z|$ have been divided by 10^{12} [A/m^2], 10^5 [A/m], and 10^8 [V/m], respectively.

wire structures at electric resonance, the induced currents in the upper and lower metal plates generated by $\vec{E}$ are parallel, so the oppositely directed induced magnetic field lines go around the metal plates and cancel within the space between the metal plates, as shown in Figs. 5(d) and 6(d). On the other hand, for nonzero sidewall-angle, cut-wire, and thin-metal wire structures, the larger the size disparity (increase of sidewall angle), the stronger the net electric dipole response in the cut-wire structure and the magnetic dipole response induced by asymmetric currents in the thin-metal wires. The reason is that for the nonzero sidewall-angled cut-wire part, the magnitude

of the vector summation of electric dipoles tends to be larger as the fabrication-induced sidewall angle increases, resulting from unbalanced current density distribution induced by $\vec{H}$. In other words, there is no longer an antisymmetric current density with respect to the xy plane through the middle of the structure, as shown in Figs. 5(a) and 6(a). This also results in an asymmetric electric field with respect to the xy plane through the middle of the structure because of the accumulated charge distribution at each metal plate, as shown in Figs. 5(c) and 6(c). For the nonzero sidewall-angled thin-metal wires part, the magnitude of the induced magnetic dipole
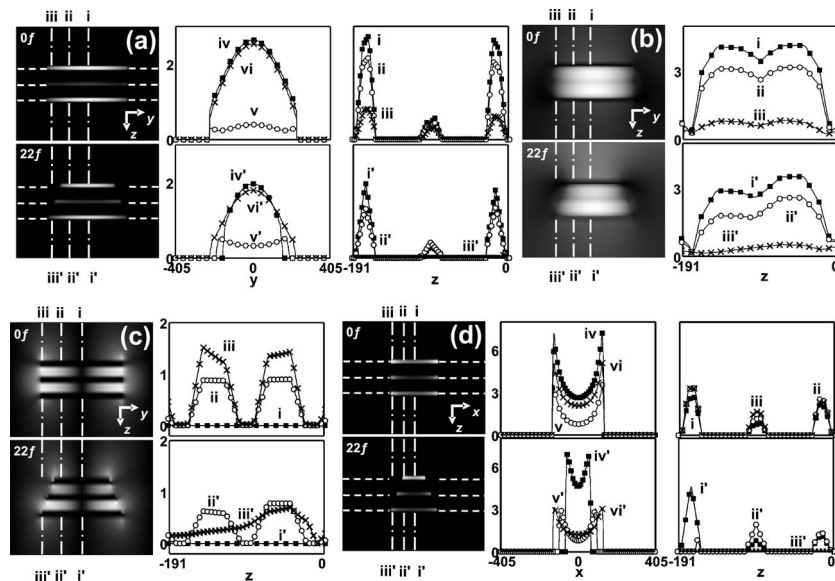

Fig. 6.   (a) Magnitude of y component of current density ($|J_y|$); (b) x component of magnetic field ($|H_x|$); and (c) z component of electric field ($|E_z|$) at a frequency of min{Re[μ_{eff}]} for two-functional-layered s-eNIM with sidewall angles (0°, 22°) are plotted along lines at the edge of cut-wire structure ($x=405$ nm). (d) $|J_y|$ along the lines in edge of thin-metal wires structure ($y=405$ nm). The values of $|J_y|$, $|H_x|$, and $|E_z|$ have been divided by 10^{12} [A/m^2], 10^5 [A/m], and 10^8 [V/m], respectively.

moment between the metal plates tends to be stronger owing to a larger differential strength of induced currents by $\vec{E}$ in the upper and lower metal plates, as shown in Figs. 5(d) and 6(d). Notice that in addition to the dependence on the sidewall angle, the antiresonant behavior of $\text{Re}(\xi)$ with the same sidewall angle as shown in Fig. 4 also becomes stronger as the number of functional layers increases [17].

4. SUMMARY

In summary, we have experimentally demonstrated the optical effects of fabrication-induced structural asymmetry (sidewall angle) in one- to three-functional-layered elliptical negative-index metamaterials embedded in a symmetric medium consisting of a glass substrate, a glass superstrate, and an index-matching liquid. Numerical simulations are in good agreement with the experiment. For application, negative-index metamaterials should be improved through minimization of the structural asymmetry to achieve the double-negative material or multifunctional layered structures (the proposed fabrication procedure was reported in [23]).

REFERENCES

1. S. Zhang, W. Fan, N. C. Panoiu, K. J. Malloy, R. M. Osgood, and S. R. J. Brueck, "Optical negative-index bulk metamaterials consisting of 2D perforated metal-dielectric stacks," Opt. Express **14**, 6778–6787 (2006).
2. Z. Ku, and S. R. J. Brueck, "Comparison of negative refractive index materials with circular, elliptical, and rectangular holes," Opt. Express **15**, 4515–4522 (2007).
3. G. Dolling, M. Wegener, and S. Linden, "Negative-index metamaterial at 780 nm wavelength," Opt. Lett. **32**, 53–55 (2007).
4. S. R. J. Brueck, "Optical and interferometric lithography—nanotechnology enablers," Proc. IEEE **93**, 1704–1721 (2005).
5. J. Valentine, S. Zhang, T. Zentgraf, E. Ulin-Avila, D. A. Genov, G. Bartal, and X. Zhang, "Three-dimensional optical metamaterial with a negative refractive index," Nature **455**, 376–379 (2008).
6. W. Wu, Z. Yu, S. Y. Wang, R. S. Williams, Y. Liu, C. Sun, X. Zhang, E. Kim, Y. R. Shen, and N. X. Fang, "Midinfrared metamaterials fabricated by nanoimprint lithography," Appl. Phys. Lett. **90**, 063107 (2007).
7. N. Liu, L. Fu, S. Kaiser, H. Schweizer, and H. Giessen, "Plasmonic building blocks for magnetic molecules in three-dimensional optical metamaterials," Adv. Mater. (Weinheim, Ger.) **20**, 3859–3865 (2008).
8. Z. Ku and S. R. J. Brueck, "Experimental demonstration of sidewall-angle-induced bianisotropy in multiple-layer negative-index metamaterials," Appl. Phys. Lett. **94**, 153107 (2009).
9. G. Dolling, M. Wegener, and S. Linden, "Realization of three-functional-layer negative-index photonic metamaterial," Opt. Lett. **32**, 551–553 (2007).
10. E. Kim, Y. R. Shen, W. Wu, E. Ponizovskaya, Z. Yu, A. M. Bratkovsky, S. Y. Wang, and R. S. Williams, "Modulation of negative index metamaterials in the near-IR range," Appl. Phys. Lett. **91**, 173105 (2007).
11. S. Zhang, W. Fan, K. J. Malloy, S. R. J. Brueck, N.-C. Panoiu, and R. M. Osgood, "Near-infrared double negative metamaterials," Opt. Express **13**, 4922–4930 (2005).
12. V. M. Shalaev, W. Cai, U. K. Chettiar, H.-K. Yuan, A. K. Sarychev, V. P. Drachev, and A. V. Kildishev, "Negative index of refraction in optical metamaterials," Opt. Lett. **30**, 3356–3358 (2005).
13. D. R. Smith, D. C. Vier, Th. Koschny, and C. M. Soukoulis, "Electromagnetic parameter retrieval from inhomogeneous metamaterials," Phys. Rev. E **71**, 036617 (2005).
14. X. Chen, B.-I. Wu, J. A. Kong, and T. M. Grzegorczyk, "Retrieval of the effective constitutive parameters of bianisotropic metamaterials," Phys. Rev. E **71**, 046610 (2005).
15. M. S. Rill, C. Plet, M. Thiel, I. Staude, G. von Freymann, S. Linden, and M. Wegener, "Photonic metamaterials by direct laser writing and silver chemical vapor deposition," Nature Mater. **7**, 543–546 (2008).
16. M. S. Rill, C. E. Kriegler, M. Thiel, G. von Freymann, S. Linden, and M. Wegener, "Negative-index bianisotropic photonic metamaterial fabricated by direct laser writing and silver shadow evaporation," Opt. Lett. **34**, 19–21 (2009).
17. Z. Ku, J. Zhang, and S. R. J. Brueck, "Bianisotropy of multiple-layer fishnet negative-index metamaterials due to angled sidewalls," Opt. Express **17**, 6782–6789 (2009).
18. Z. Li, K. Aydin, and E. Ozbay, "Determination of the effective constitutive parameters of bianisotropic metamaterials from reflection and transmission coefficients," Phys. Rev. E **79**, 026610 (2009).
19. CST Studio Suite 2006B, ⟨www.cst.com⟩.
20. M. A. Ordal, L. L. Long, R. J. Bell, S. E. Bell, R. R. Bell, R. W. Alexander, and C. A. Ward, "Optical properties of the metals Al, Co, Cu, Au, Fe, Pb, Ni, Pd, Pt, Ag, Ti, and W in the infrared and far infrared," Appl. Opt. **22**, 1099–1120 (1983).
21. D. R. Smith, S. Schultz, P. Markoš, and C. M. Soukoulis, "Determination of effective permittivity and permeability of metamaterials from reflection and transmission coefficients," Phys. Rev. B **65**, 195104 (2002).
22. J. B. Pendry, A. J. Holden, W. J. Stewart, and I. Youngs, "Extremely low-frequency plasmons in metallic mesostructures," Phys. Rev. Lett. **76**, 4773–4776 (1996).
23. A. Boltasseva and V. M. Shalaev, "Fabrication of optical negative-index metamaterials: recent advances and outlook," Metamaterials **2**, 1–17 (2008).